Direct numerical simulations of transonic flow around an airfoil at moderate Reynolds numbers.

Markus Zauner* and Nicola De Tullio†
University of Southampton, Southampton, Hampshire, SO17 1BJ, United Kingdom

Neil D. Sandham‡
University of Southampton, Southampton, Hampshire, SO17 1BJ, United Kingdom

In order to reduce friction and wave drag on the wings of more efficient next generation aircraft, it is important to understand laminar-turbulent boundary-layer transition and shock-wave interactions. In this contribution, fully-resolved direct numerical simulations of Dassault Aviation's V2C profile at transonic conditions and a Reynolds number of half a million are presented. Kelvin-Helmholtz instabilities appear in the shear layers on the pressure- and suction-sides, followed by a self-sustained laminar-turbulent transition process promoted by the stretching of rib vortices between larger co-rotating structures. Multiple acoustic structures interacting with the boundary layer are also observed, together with upstream-propagating shock waves. Regions of flow separation on the suction side exhibit unsteadiness with Strouhal numbers in the range of $St \approx 0.5 - 0.6$. This is distinct from a standing wave oscillation in lift at $St = 0.12$, which agrees well with transonic buffet frequencies, reported for experiments on the same airfoil at higher Reynolds numbers. The insensitivity of the principal results to the chosen grid resolution and spanwise domain size is carefully established.

Nomenclature

Re	=	Reynolds number
M	=	Mach number
$St = \frac{f \cdot c}{U_\infty}$	=	Strouhal number
Pr	=	Prandtl number
$C_p = \frac{2(p-p_\infty)}{\gamma p_\infty M^2}$	=	Pressure coefficient
$C_{p,crit}$	=	Critical pressure coefficient
C_f	=	Skin-friction coefficient
C_L	=	Lift coefficient

*PhD Candidate, Aerodynamics and Flight Mechanics Group, m.zauner@soton.ac.uk
†Former Post Doctoral Researcher, Aerodynamics and Flight Mechanics Group, N.De-Tullio@soton.ac.uk
‡Professor, Aerodynamics and Flight Mechanics Group, n.sandham@soton.ac.uk

C_D	=	Drag coefficient
C_{Suth}	=	Sutherland constant
γ	=	Specific heat ratio
μ	=	Dynamic viscosity
TKE	=	Turbulent kinetic energy
x, y, z	=	Cartesian coordinates
ξ, η, ζ	=	Curvilinear coordinates
s	=	Surface distance
α	=	Angle of attack
c	=	Axial chord length
q^*	=	Dimensional quantity
q	=	Dimensionless quantity
$\widetilde{q}$	=	Favre-averaged quantity
$\overline{q}$	=	Mean quantity
q'	=	Fluctuation around the mean value
q_∞	=	Dimensionless quantity at freestream conditions
q_w	=	Dimensionless quantity at wall
U, V, W	=	Dimensionless velocity components
p	=	Dimensionless pressure
ρ	=	Dimensionless density
ω	=	Vorticity
T	=	Dimensionless temperature
t	=	Dimensionless time
Δt	=	Time step
$TU = \frac{c}{U_\infty}$	=	Dimensionless time unit
λ	=	Wave length
f	=	Frequency
$\omega_r = 2\pi f$	=	Angular frequency
$c_{ph} = \lambda f$	=	Phase speed
a	=	Speed of sound
a_u	=	Upstream propagation speed of sound
ϕ	=	Wave angle

Δn = Wall-normal grid spacing

Δs = Wall-tangential grid spacing

Introduction

Transonic flow over aircraft wing sections exhibits a plethora of highly complex flow phenomena that have attracted attention for several decades. The first experiments on the transonic flow around airfoils were conducted already in 1934[1], with fundamental research in the field of transonic wing aerodynamics carried out in the early second half of the 20^{th} century. A comprehensive review of the early work on transonic wings is provided by [2]. Since the first transonic flights in 1944, pilots of aircraft approaching transonic speeds repeatedly reported flutter phenomena that affected the aeroelastic stability of the aircraft[3]. Transonic buffet is characterized by a structural response to an aerodynamic excitation produced by separated flows interacting with shock waves. It is of great interest to be able to define buffet-boundaries as precisely as possible in order to fully exploit and potentially extend the safe flight envelope. However, despite large experimental efforts, the self-sustained flutter mechanism is still not fully understood[4][5]. Significant oscillations of aerodynamic loads can also be observed on rigid wings[6], so it is generally assumed that the structural response of the wing is triggered by resonance effects after the disturbance amplitude reaches a sufficient magnitude.

With the rise of computational fluid mechanics, many phenomena have been studied in detail by direct numerical simulations (DNS) in simplified configurations. Recent advances in large-scale computing and increasing performance of algorithms for solving systems of partial differential equations motivate high fidelity simulations that are now feasible for complete airfoil test cases. The Reynolds number and spanwise domain width are limiting factors in such simulations. After the two-dimensional (2D) study of the flow over a transonic airfoil at Reynolds numbers up to Re = 10,000 by [7], a series of 2D studies (e.g. [8],[9]) were carried out.

Besides incompressible 3D simulations up to high Reynolds numbers (e.g. [10]), large eddy simulations including sub-grid scale models have been performed (e.g. [11],[12]), but will not be discussed here in detail. Due to significantly higher costs, only a few studies have involved fully-resolved DNS to date. The first 3D DNS study of a transonic airfoil at Reynolds numbers up to Re = 10,000 was performed by [13]. Considering a low Mach number of M = 0.2, [14] pushed the Reynolds number for a 3D DNS of a NACA0012 airfoil to micro air vehicle (MAV) conditions, whereas [15] considered Mach- and Reynolds-numbers up to M = 0.8 and Re = 50,000, respectively. An extensive grid dependency study of the well known NACA0012 airfoil was conducted by [16] for a moderate Reynolds number of Re = 500,000 and a Mach number of M = 0.65, considering seven grids up to one billion points and a domain width of 10% of the axial chord c. Aerodynamic coefficients and boundary-layer parameters showed only small differences for different meshes, whereas significant differences in the turbulent kinetic energy (TKE) spectrum were reported for structures at

higher frequencies and wavenumbers. Even though the grid study showed only partial convergence, a fully-resolved DNS was not expected to show significantly different behavior, as the initial subrange of the TKE spectra is, for the fine grids, at least partially resolved. A DNS for the same airfoil by [17] considered a low Mach number of $M = 0.2$ at a Reynolds number of one million with the biggest grid of about 0.8 billion points for a circular domain with a radius of 15 times the chord length and a spanwise domain size of $0.2c$.

The simulations in the current contribution aim to extend the DNS database of fully-resolved transonic flow over aircraft-wing sections. Dassault Aviation's V2C laminar-flow wing profile is analyzed at a fixed inclination of $\alpha = 4°$, considering a Mach number of $M = 0.7$ and a Reynolds number of $Re = 500{,}000$. This airfoil was the subject of experimental[18][19] as well as numerical studies[11][12] in the course of the TFAST project* (part of EU's Horizon 2020 programme). In experiments at considerably higher Reynolds numbers[18], the onset of transonic buffet was observed at similar angels of attack as the one reported in the present contribution. The simulations also potentially provide baseflows for future local and global stability analysis to link the self-sustaining buffet mechanism to a global instability[20].

We will start with the introduction of applied methods regarding direct numerical simulations and grid generation. Before justifying the grid resolution, the results will be discussed so that the key flow features are identified. The conclusions are summarized in the last section.

Methodology

Direct numerical simulations

Direct numerical simulations are carried out using the high-order fully-parallelized multi-block finite difference in-house code SBLI[21]. For the spatial discretisation of the flowfield, a fourth order finite difference scheme is applied in combination with a Carpenter scheme[22] at the boundaries. The dimensionless Navier-Stokes Equations (NSE) are solved in time employing a low-storage third-order Runge-Kutta scheme. Velocity, temperature and density at freestream conditions define the reference quantities, while the characteristic length scale is denoted by the axial chord length of the airfoil. The fluid is assumed as Newtonian with a specific heat ratio and Prandtl number of $\gamma = 1.4$ and $Pr = 0.72$, respectively. The temperature dependency of the dynamic viscosity is modeled by Sutherland's law according to

$$\mu = T^{\frac{3}{2}} \frac{1 + C_{Suth}}{T + C_{Suth}}, \tag{1}$$

where the Sutherland constant is set to $C_{Suth} = 0.41$. The isothermal wall-temperature is set to free-stream temperature ($T_w = 1$). Integral characteristic boundary conditions[23] are applied to avoid reflections of shock- and pressure-waves at the domain boundaries. At the outlet, zonal characteristic boundary conditions[24] are applied using between 31 and

*http://tfast.eu/

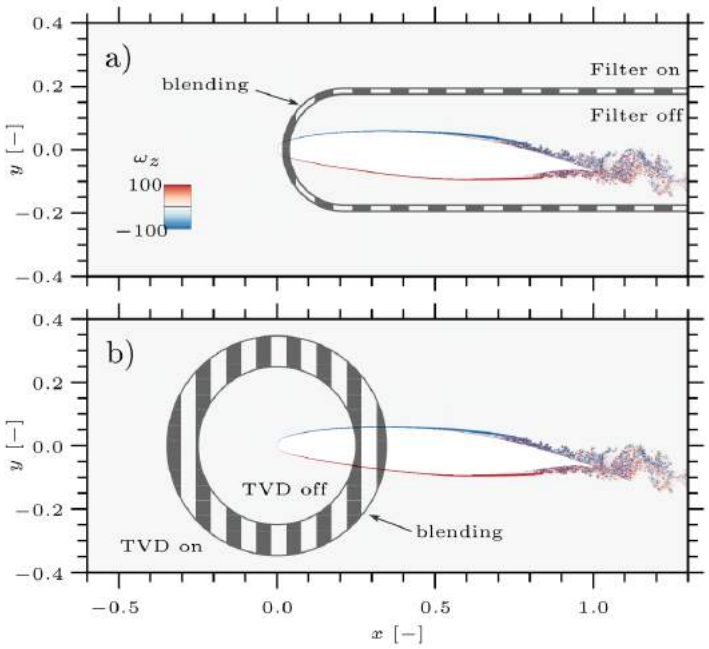

Fig. 1 Active regions for (a) 6^{th} order filter and (b) TVD scheme.

51 grid points near the outflow.

A total variation diminishing (TVD) scheme, in combination with an implicit 6^{th}-order filter in the farfield (figure 1(a)), increases the numerical stability of the simulation near shock waves and suppresses spurious disturbances. The TVD scheme is disabled near the wall (within the 6 closest points in wall-normal direction) and around the leading edge (LE) according to figure 1(b), as there are no shock waves expected and it causes artificial disturbances at the stagnation point, as shown in figure 2(a). Without additional filtering, strong disturbances occur around the leading edge (figure 2(b)). A 2D study suggests that upstream-propagating pressure waves cause grid-to-grid point oscillations in the farfield between the LE and the inlet. These oscillations are observed to perturb the freestream and cause downstream-convecting spurious structures that eventually get resolved by the finer grid near the leading edge. As shown in figure 2(c), spurious structures even occur for refined grids without the filter.

Applying the filter every 50 time steps is sufficient for a clean freestream even for a small margin of $-0.1 < \omega_z < 0.1$ as shown in figure 2(d). Structures with $|\omega_z| \approx 0.1$ correspond to fluctuations of about $v' \approx 10^{-5}$ in the wall-normal velocity component and about $u' \approx 5 \cdot 10^{-5}$ in the wall-tangential velocity component (assuming a grid spacing of $\Delta n = 10^{-4}$ and $\Delta s = 5 \cdot 10^{-4}$ in the wall-tangential and wall-normal directions, respectively). In addition, a localized filter technique is applied at the singular points at both corners of the blunt trailing edge, according to the trailing edge treatment of [25].

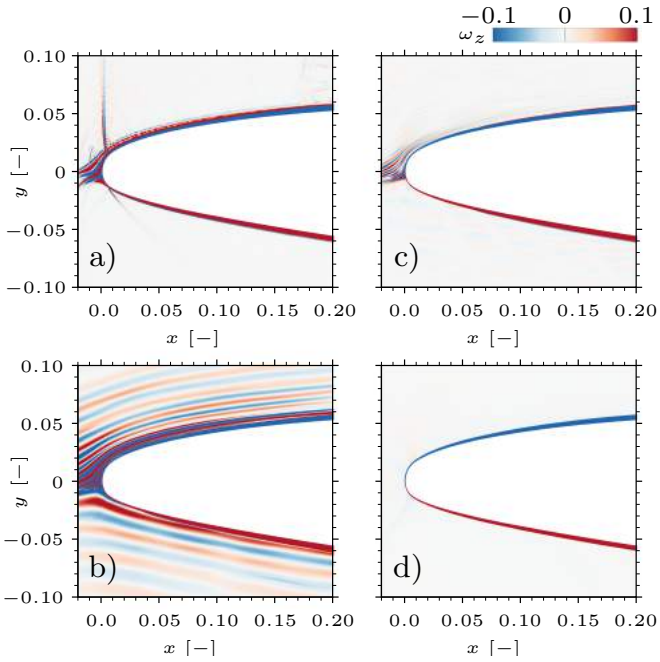

Fig. 2 Contours of the z-vorticity for different test cases to visualize the effects of different TVD and 6^{th}-order filter configurations.

Grid generation

DNS are carried out after splitting the computational domain into three blocks consisting of one C-block (B2) around the airfoil geometry and two H-type blocks (B1 and B3) enclosing the wake region and outflow. The arrangement of all three blocks is sketched in figure 3(a). The three interfaces between $B1$ and $B3$, $B2$ and $B1$ as well as $B2$ and $B3$ are shown in the close up of figure 3(a), where the coordinates of the Cartesian coordinate system are denoted by x and y in the freestream direction and normal to it, respectively. Curvilinear coordinates are denoted by ξ and η in the circumferential and radial direction, respectively. Curves that consist of grid points with constant values of η are called ξ-gridlines, whereas curves of constant ξ-values are denoted as η-gridlines (the grey-dashed line in figure 3). High-order DNS require continuous metric terms up to the second order derivatives. This can be problematic across block boundaries for geometries with a blunt trailing edge in a three-block CH-grid domain. Furthermore, simulations at moderate or high Reynolds numbers have highly refined grids near shear- and boundary-layers, whereas the freestream requires a lower grid density. Grid solvers tend to shift points from high-resolved to lower-resolved regions to improve grid smoothness. An in-house grid generator was therefore developed to increase the control and flexibility in the distribution of grid points. The ξ-spacing and the angles of η-gridlines along domain boundaries are defined by high-order polynomials. On the one hand, high-order polynomials can be exactly defined at boundaries and therefore allow a segmentation of the airfoil surface without creating discontinuities. On the other hand, the shape is hard to control. Blending procedures are therefore applied in order to combine the advantages of high-order polynomials at the ends of each segment, with low-order functions in between. The shape of the η-gridlines is defined by blending

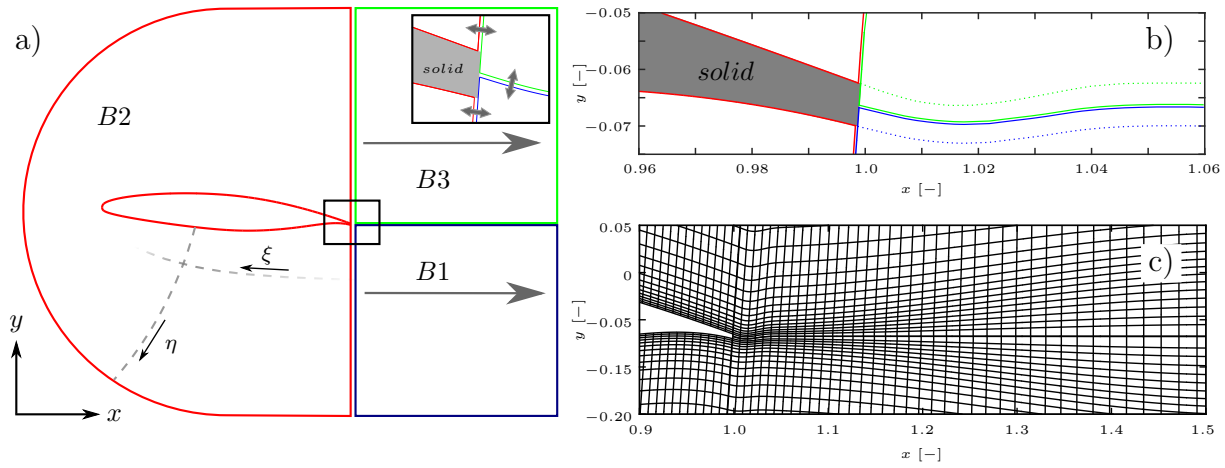

Fig. 3 (a) Segmentation of the grid into three blocks. (b) Illustration of wall gridline extensions for block 1 (blue dotted curve) and block 3 (green dotted curve). (c) Wake region of reference grid *Nc*.

a wall-optimized polynomial and an outer-boundary-optimized polynomial, so that the spacing at surfaces and outer boundaries can be defined independently and the freestream resolution is more uniform compared to grids with linear η-gridlines. The resolution along η-gridlines is defined by polynomials in the same way as the spacing in the ξ-direction at boundaries. The ξ-gridlines in $B1$ and $B3$ that pass through both corners of the blunt trailing edge are designed as smooth continuations of the airfoil surface, as indicated by the dotted curves in figure 3(b). Those gridlines slightly diverge with increasing distance from the airfoil, so that the grid resolving the wake becomes more homogeneous (figure 3(c)). Towards the outflow of $B1$ and $B3$ the grid has a Cartesian topology and is only stretched in the x-direction. More details on the grid-generation process and the applied open-source tool are provided in [26]. A parameter study performed in [27] suggests that a radius of the C-block between $5.3c < R < 7.3c$ is sufficient to capture the potential flow around an airfoil at $Re = 5 \cdot 10^4$ and $M = 0.4$. In the current work, the radius is set to $R = 7.5c$ for all simulations. The domain extent of $B1$ and $B3$ in the x-direction is set to $5c$[27]. A constant time step of $\Delta t = 2 \cdot 10^{-5}$ time units ($TU = c/U_\infty$) is maintained for all the simulations presented in this work. Table 1 gives an overview of all simulations and key parameters. A reference case ($C0$) with a spanwise domain extent of $L_z = 0.05c$ (note that the maximum wall-distance of the shear layers due to the separated flow on the suction side is about $n_{shear,max} \approx 0.017c$) is run for 25 time units.

A study of the spanwise domain size effect on the transitional flow around airfoils with $0.1 \leq L_z \leq 0.8$ by [28] shows that the spanwise domain size has negligible effect on the mean aerodynamic quantities. In order to confirm that the narrow domain case still captures the main flow-phenomena an additional simulation ($C1$) with a five times wider domain is carried out in the present work. Grid refined simulations ($G1$ and $G2$) will be discussed later in section V, after we discuss the important flow features. All simulations are run on the Tier-1 UK national supercomputing facilities

Tag	*Grid*	L_z	N_z	N_{total}	*Re*	*M*	α	*Runtime*	*Core hours*	*Remarks*
*C*0	*Nc*	0.05	150	$1.07 \cdot 10^9$	500,000	0.7	4°	25 *TU*	$3.6 \cdot 10^6$	reference case
*C*1	*Nc*	0.25	750	$5.35 \cdot 10^9$	500,000	0.7	4°	8 *TU*	$5.6 \cdot 10^6$	extended domain
*G*1	*Od*	0.05	150	$1.68 \cdot 10^9$	500,000	0.7	4°	8 *TU*	$1.2 \cdot 10^6$	refined $x-y$-plane
*G*2	*Nc*	0.05	250	$1.78 \cdot 10^9$	500,000	0.7	4°	8 *TU*	$1.7 \cdot 10^6$	refined in z-direction

Table 1 Overview of the different cases run on ARCHER and key parameters treated in this contribution.

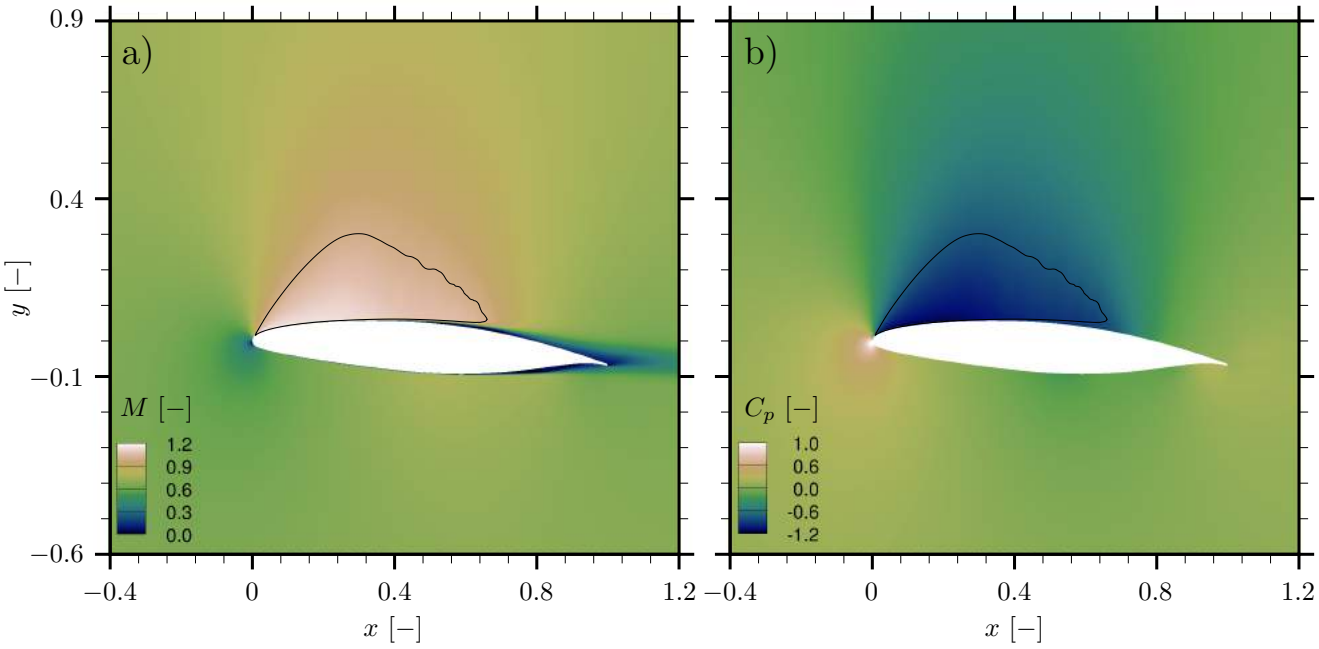

Fig. 4 Contour plots showing time- and span-averaged Mach number (a) and pressure coefficient C_p (b) averaged over 25 time units. The black curve denotes the sonic line.

ARCHER [†]. A typical job employing 1270 nodes (30480 cores) on ARCHER for about 14 hours uses about 0.4 million core hours to cover three time units.

Results

Figure 4 shows the local Mach number (a) and pressure coefficient (b) of the time- and span-averaged flowfield of case *C*0 (see table 1). The black sonic line in figure 4(a) bounds a region of supersonic flow covering ~ 70% of the suction side. The acceleration of the flow causes significantly decreased pressure values within the first quarter of the suction side of the airfoil, before the pressure starts recovering again (figure 4(a)). This is also observed in figure 5(a), showing the averaged pressure coefficient C_p as a function of the axial chord position. The dotted line denotes the

[†]http://www.archer.ac.uk/about-archer/

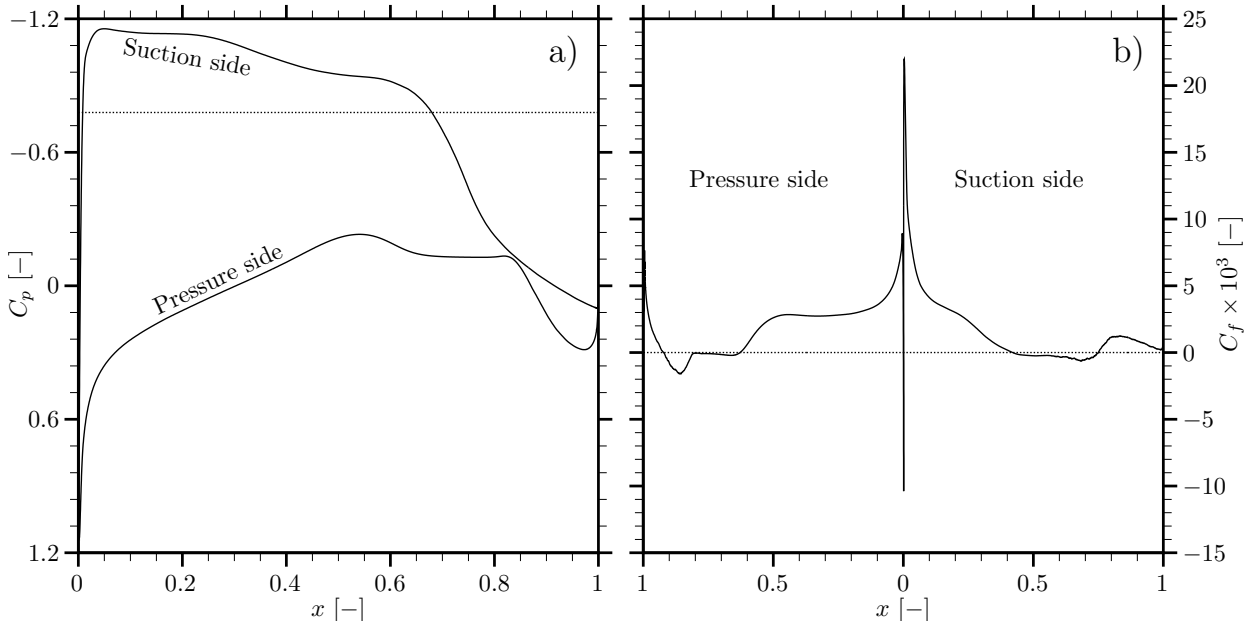

Fig. 5 Time- and span-averaged pressure coefficient C_p (a) and skin-friction coefficient C_f (b) after 25 time units. The dotted lines indicate (a) the critical pressure coefficient of $C_{p,crit.} = 0.779$ and (b) the zero-line of C_f.

critical pressure coefficient to highlight again the supersonic region over the suction side. The steep drop of the C_f on the suction side coincides with the flow recirculation that is indicated by the negative average skin-friction coefficient in figure 5(b). A regime of separated flow is also present on the pressure side near the TE.

To identify the time-dependent features, figure 6 shows the instantaneous skin-friction coefficient on the suction surface as a function of time and axial chord position for the reference case $C0$ (figure 6(a)) and grid-refined simulations $G1$ (figure 6(b)) and $G2$ (figure 6(c)) over an interval of 8 time units. For now, we will focus on figure 6(a), as the remaining plots in figure 6 will be discussed in the grid dependency study in section V. The line plot on top of the C_f-contour marks the proportion of time the flow is separated, as a function of the axial chord position. Despite the positive time-averaged C_f values in the last quarter chord of the airfoil ($t_{sep}/8 < 50\%$), intermittent flow separation is present. The orange stripes in figure 6(a) correspond to two dimensional Kelvin Helmholtz (KH) roll-ups that grow in the shear layer, while convecting downstream with a phase speed of $c_{ph} \approx 0.73$. [27] also reported the formation of KH roll-ups, at lower Reynolds numbers. The wavelength measured at half chord is approximately $\lambda \approx 0.0365$, suggesting an angular frequency of $\omega_r \approx 125.7$ that corresponds to Strouhal numbers of $St = fc/U_\infty = \omega_r/(2\pi) \approx 20$. Similar distinctive frequencies were reported in [29] for the flow over a high-pressure turbine vane at similar flow conditions as those reported here. A linear stability analysis by [30] later revealed that these unsteady flow features are manifestations of linear boundary-layer instabilities. Changes in the boundary layer thickness and variations in the separation line (sketched in figure 6(a) by the red curve) also impact the development of KH roll-ups. With earlier and stronger flow separation, KH instabilities evolve earlier and form stronger vortices that can even induce counter-rotating vortices

close to the wall surface. After the turbulent breakdown, strong large-scale vortices are present, which interact with the potential flow and each other. When the ratio of vortex-core size over core distance between two co-rotating vortices exceeds a critical value[31], such structures merge to larger, unstable structures (light-blue framed structure in figure 6(a)). Furthermore, local minima of C_f in figure 6(a) are highlighted by white $\times$-symbols and occur with a frequency of $St \approx 0.5$. The pressure side of the airfoil shows similar characteristics.

The pseudo-Schlieren contour-plot in figure 7(a) shows the pressure gradient magnitude ($||\nabla p||$) of the instantaneous flowfield and illustrates the generation of acoustic waves (AW) by multiple sources in the aft-section on both sides of the airfoil. Significant emitters are the big turbulent vortices convecting downstream over the airfoil and into the wake[32]. Furthermore, those structures interact with the trailing edge and generate back-scattered waves[33]. Pressure waves (PW), often called Kutta waves[34], travel upstream over the suction surface. As they approach the supersonic region, they slow down and appear to coalesce near the sonic line. Eventually, upstream-propagating shock waves (SW) form. Due to the rising pressure levels immediately downstream of the shock wave, the shock position has to move in order to satisfy the shock conditions[35]. While moving upstream, the shock wave tilts, causing a reflection shock at the wall. Approaching the leading edge, the shock waves weaken and eventually emit strong acoustic pressure waves from the leading edge into the farfield upstream of the airfoil. As the flow in the freestream is subsonic, pressure waves can also circumvent the supersonic region. Sliding upstream along the sonic line, they introduce disturbances into the supersonic region (indicated by the dotted magenta curve in figure 7(a)). All this results in a complex interaction between shock- and pressure-waves and the boundary layers, causing an unsteady behavior of recirculation areas. From the upstream contour of C_f in figure 6, the Strouhal number is $St \approx 0.5$, since four local minima (white $\times$-symbols) are observed at half chord within 8 time units. Spectra of the wall-density at representative chord positions corresponding to case $C0$ are shown by [36].

The KH structures are also captured by plotting Q-criterion surfaces colored by vorticity in figure 7(b). Laminar flow on the suction side is maintained up to $x \approx 0.65$ (figure 6). A transition mechanism similar to [27] is observed, where vortex stretching of longitudinal vortices by strong 2D roll-ups promotes rapid turbulent breakdown. These counter-rotating longitudinal vortex structures are called ribs [37] and arise from a secondary instability, caused by the 2D KH roll-ups [38][39][40]. Close to the surface, figure 7(b) shows also weak vortical structures that are convecting slowly upstream within the separated boundary layer. In simulation $C1$, with a five times wider domain, early KH structures are still 2D. The snapshot in figure 8 shows the transition region on the upper surface ($0.5 < x < 0.65$) of the wide-domain case $C1$. Rib vortices are observed between the first two 2D roll-ups. However, the characteristics of the main flow phenomena, observed in figure 8 for the wide domain case, are also present in the reference case (figure 7(b)).

The significantly separated boundary layers also allow acoustic waves, caused by the turbulent breakdown, to move upstream close to the wall. On the pressure side, the relative velocity to the potential flow outside the boundary layer is supersonic and disturbances emitted into the freestream show a Mach-like wave pattern (labeled in figure 7(a) as MW).

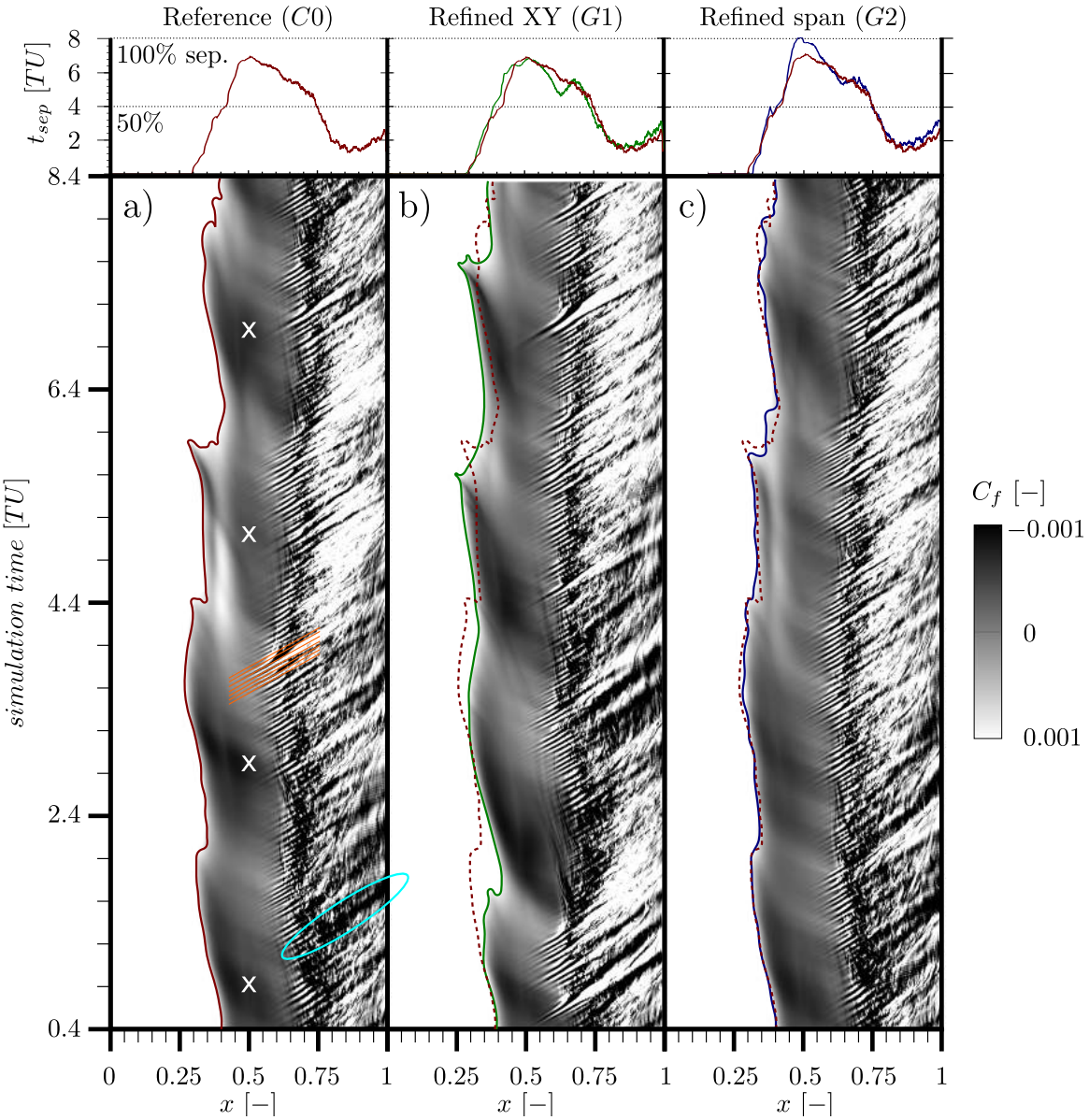

Fig. 6 Contour plots showing the instantaneous skin-friction coefficient over the suction side at a fixed spanwise position as a function of space and time. Top line plots show the proportion of time the flow is separated.

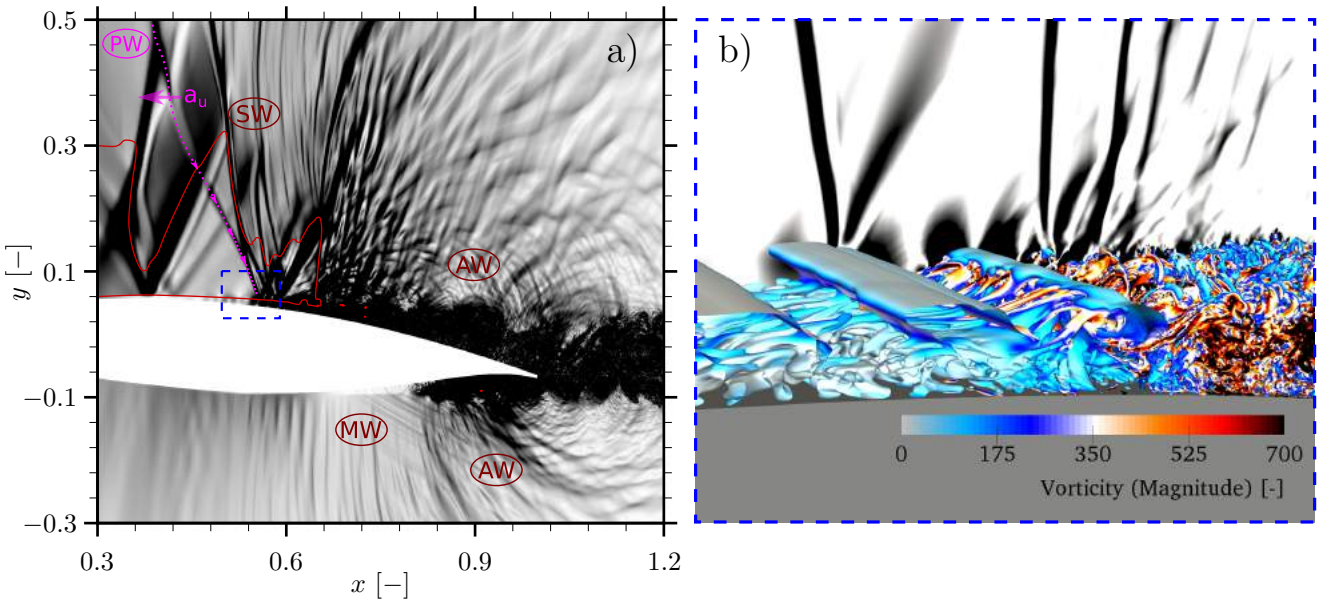

Fig. 7 (a) Pseudo-Schlieren plot of the pressure gradient magnitude and (b) Q-criterion surfaces of vortex structures colored by vorticity magnitude.

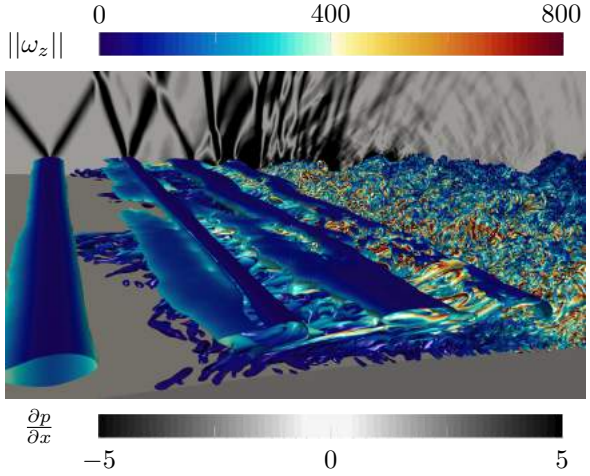

Fig. 8 Snapshot of case $C1$ at $t = 8$ showing Q-criterion surfaces ($Q = 200$) coloured by vorticity magnitude. Black regions in the background indicate high axial pressure gradients.

Considering that the upstream phase speed of the disturbances in the boundary layer is $c_{ph} = 1.47$ (the sum of local sonic speed and recirculation speed) and the wavelength is $\lambda = 0.0062$ (measured from a snapshot at $x \approx 0.52$), the resulting Strouhal number is $St \approx 237$. The wave angle ϕ_{Mach} can be calculated according to

$$\phi_{Mach} = \arctan\left(\frac{a}{a + u_{rev} + u_e}\right), \tag{2}$$

where a denotes the speed of sound, while u_e and u_{rev} denotes boundary-layer edge velocity and the velocity of reverse flow, respectively. The calculated value of $\phi_{Mach,calc} = 25.1°$ agrees well with the measured value of $\phi_{Mach,m} = 24.3°$.

Besides such high-frequency acoustic structures, the simulations also contain important low-frequency phenomena. The top plot of figure 9 shows the lift coefficient as a function of time. A distinct low-frequency cycle can be observed at a Strouhal number of $St = 0.12$, which is distinct from the $St \approx 0.5$ found earlier for the skin-friction behavior (figure 6). Oscillations with $St = 0.12$ are clearly visible in wall-density fluctuations at multiple locations along the airfoil as well. Since the non-dimensional temperature at the isothermal airfoil surface is constant and equal to unity, the wall pressure is proportional to the wall density according to

$$p_w = \frac{\rho_w}{\gamma M^2}. \tag{3}$$

Figure 9 also shows representative wall-density signals starting at the lower trailing edge (red), going around the leading edge (green) and ending at the upper trailing edge. A phase shift in the signals can be observed, while the low-frequency cycle seems to vanish near the half-chord on the upper surface (light blue curve). The envelope, sketched by dotted lines, corresponds to approximately one $St = 0.12$ low-frequency cycle and is reminiscent of a modulation of the separated boundary-layer breathing phenomenon at $St \approx 0.5$. The wall-density signal contains a wide range of flow-phenomena, the envelope behaviour is less obvious at other times. A high-frequency event can be observed around 20 time units, where the breathing of the separation bubble is such that breakdown events develop at locations further upstream ($x < 0.5$). Applying a spectral low-pass filter allows us to plot in figure 10 the density fluctuation around the mean value with $St < 0.3$, as a function of surface distance from the leading edge at different time steps between a local lift minimum at $t = 11$ (blue) and maximum at $t = 16$ (red). A standing wave pattern appears over the suction as well as pressure side. A node in the standing wave pattern near half-chord explains why the low-frequency cycle cannot be observed in the local wall-density signal, as mentioned before. Experimental studies of [19] analyzing the $V2C$ airfoil at Mach numbers and Reynolds numbers about $M \approx 0.7$ and $Re \approx 1.8 \cdot 10^6$, respectively, suggested buffet frequencies between $St = 0.12 - 0.16$ ($f = 290 - 370\ Hz$) at zero-incidence. Due to tunnel confinement effects, no buffet could be observed at higher angles of attack. [18] reported buffet frequencies at higher Reynolds numbers ($Re \approx 2.85 \cdot 10^6$) and an angle of attack of $\alpha = 4°$ between $f = 85.4 - 137Hz$ considering wings twice as long as [19] with degraded surface

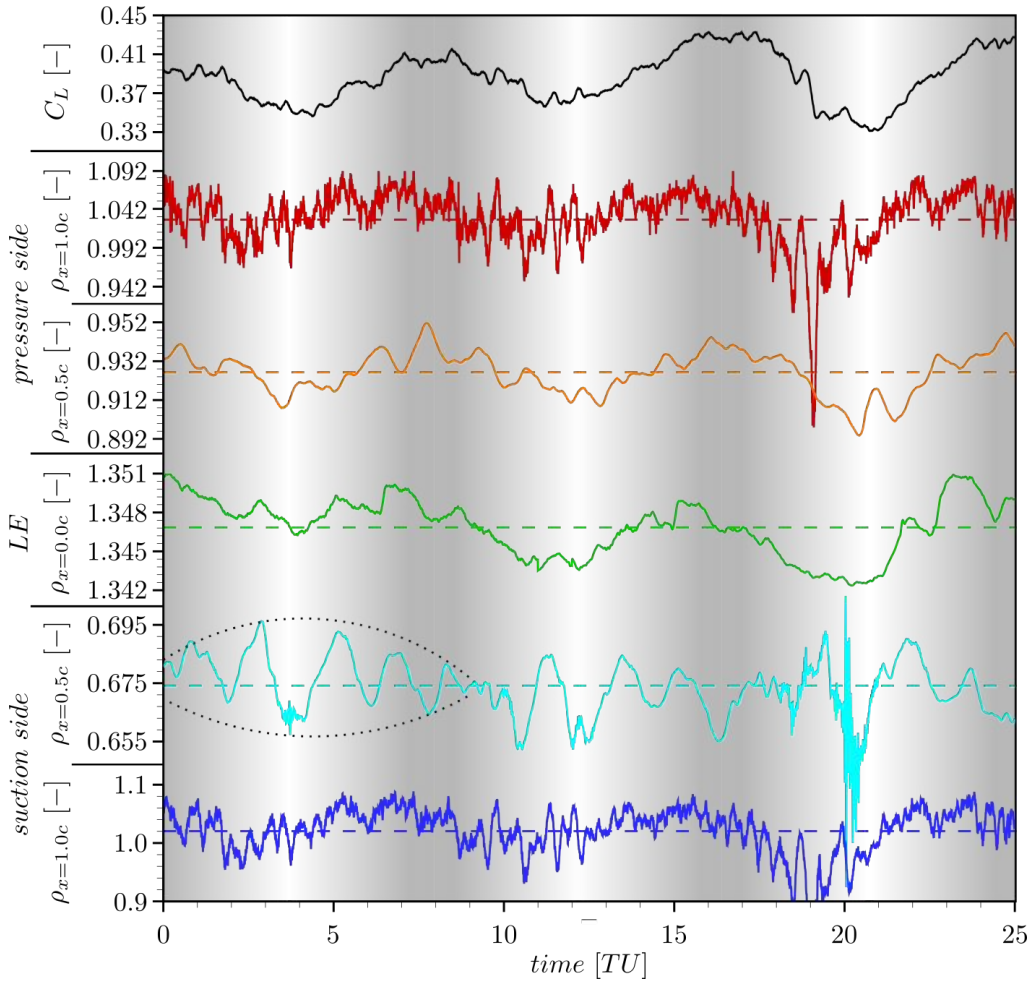

Fig. 9 Lift coefficient and wall-density at several axial positions as a function of time.

quality and polished surface, respectively. Assuming similar viscosity for both experiments, the Strouhal numbers of buffet phenomena in [41] are $St \approx 0.09 - 0.14$. Even though the experiments were carried out at significantly higher Reynolds numbers showing permanent shock waves, the suggested buffet frequencies agree well with the low-frequency phenomenon at $St \approx 0.12$ in the current work.

Grid study

The reference grid is denoted by *Nc* and consists of more than one billion points with a spanwise domain extent of 5% of the chord length (Table 1). The irrotational freestream conditions are adequately recovered at the domain boundaries (with density fluctuations within 1% of ρ_∞) and no severe boundary reflections are observed. To confirm the convergence of the time- and span-averaged flowfield of case *C*0, the variance of the time-averaged density as a

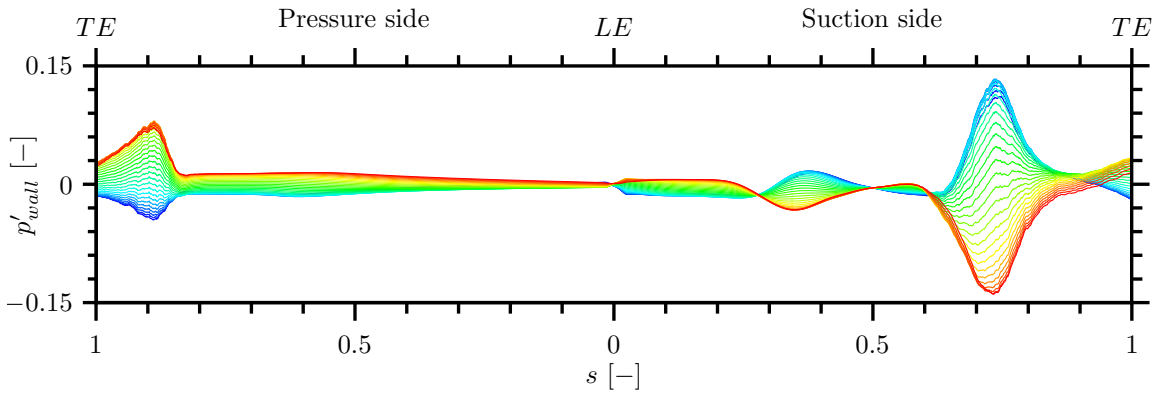

Fig. 10 Deviation of the instantaneous wall-pressure from the time averaged value against surface distance (s) for different time steps in half of a low-frequency cycle between $t = 11$ (blue) and $t = 16$ (red).

function of the spanwise position, is calculated for every grid point in the xy-plane according to

$$var_\rho = \frac{1}{N_z}\sum_{i=1}^{N_z}(\tilde{\rho}_i - \tilde{\bar{\rho}})^2, \tag{4}$$

$$with\ \tilde{\bar{\rho}} = \frac{1}{N_z}\sum_{i=1}^{N_z}\tilde{\rho}_i, \tag{5}$$

where N_z is the resolution in the spanwise direction. Figure 11 shows the maximum values of the spanwise variance in density of the time- and span-averaged flowfield at different run times. Ideally, var_ρ should be zero for the time- and span-averaged flowfield of a simulation that is run for an infinite time, as we have spanwise periodic boundary conditions. In other words, each xy-slice of the 3D time averaged flowfield ought to be the same for a perfectly converged time-averaged flowfield. Even though the simulation captures only three cycles of the low-frequency phenomenon, the variance drops after a run time of 15 time units to values below 10^{-5}.

The grid study is performed in two steps. First, the xy-plane is refined (grid *Od* in table 1) keeping the spanwise resolution unchanged (case *G*1), whereas in a second step, the reference grid is refined only in the spanwise direction by 67% (case *G*2). The refinement in the xy-plane was guided by an error-indicator analysis[42] of the instantaneous 3D flowfield of the reference case. The Fourier spectrum of the vorticity in cubic subdomains was calculated and analyzed for high-frequency structures that do not decay with a specified rate, as would be expected for Kolmogorov microscales. Amplitudes that decrease with a lower rate are more likely to be linked to grid-to-grid point oscillations rather than being physically-important turbulent structures. The severity of the estimated error is categorized into four levels between zero (low error) and three (high error). The applied 6^{th}-order filter does not affect this method, as the critical regions are in zones where the filter is disabled. The two highest levels are plotted in figure 12 and colored orange and red for level 2 and 3, respectively. Regions with high error-severity levels are detected in the shear layers, especially in the laminar/turbulent transition zones on the pressure and the suction sides. The grid was therefore refined significantly in

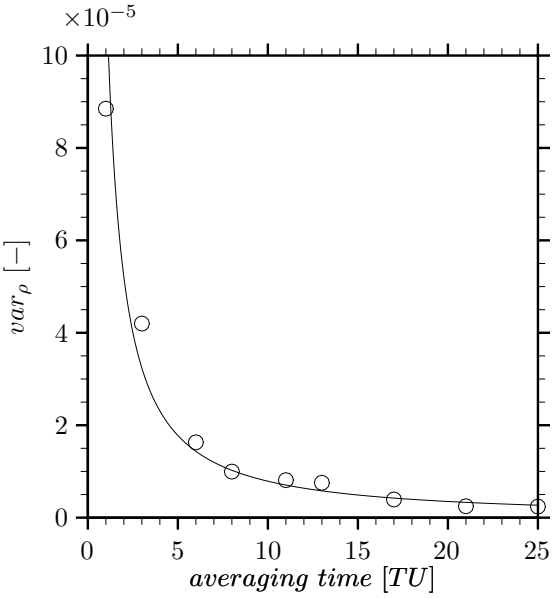

Fig. 11 Maximum variance of the density in the spanwise direction (equation 4) as a function of averaging time.

the boundary- and shear-layers on both sides. Figure 13(b) shows an overview of the refined regions, comparing the local cell size between grid *Nc* and grid *Od*. The solution of the reference simulation was then interpolated onto the refined grid *Od*. A Delaunay triangulation is applied, using the *SciPy Qhull* library [43] to identify vertices of the three closest points of grid *Nc* forming a triangle around each point of the new grid *Od*. Furthermore, the points of each vertex were weighted by their distance from the new point within the triangle. Subsequently, the quantities of each point in the new grid were calculated by a multiplication of the values of the old points, forming the vertices, with their corresponding weight-factor. This procedure is based on the *Griddata* function of the *SciPy* library and optimized for our application. In order to assess the spanwise resolution, simulation *G*2 was restarted from the solution obtained with the reference grid *Nc* and advanced in time using a grid with more than 60% additional points across the span. The spanwise interpolation from the reference solution was accomplished by a Fourier transformation of the conservative variables in the spanwise direction, zero-padding of the Fourier spectrum and finally transforming back to physical space. The suction side seems to be more critical regarding the resolution and is therefore chosen for a comparison between the instantaneous behavior of the three simulations. Figure 6 shows contour plots of the skin friction C_f along the suction side as a function of space and time, where white and black regions indicate attached and separated flow, respectively. Even though there are initial errors introduced by the low-order interpolation scheme, the main characteristics, including the low-frequency cycle, are clearly visible in all simulations. The separation lines are sketched by solid colored curves, whereas the red curve, corresponding to the reference solution, is also plotted as a dotted curve in the refined cases. The period of the $St \approx 0.5$ cycle does not change significantly and also the separation and transition locations agree well

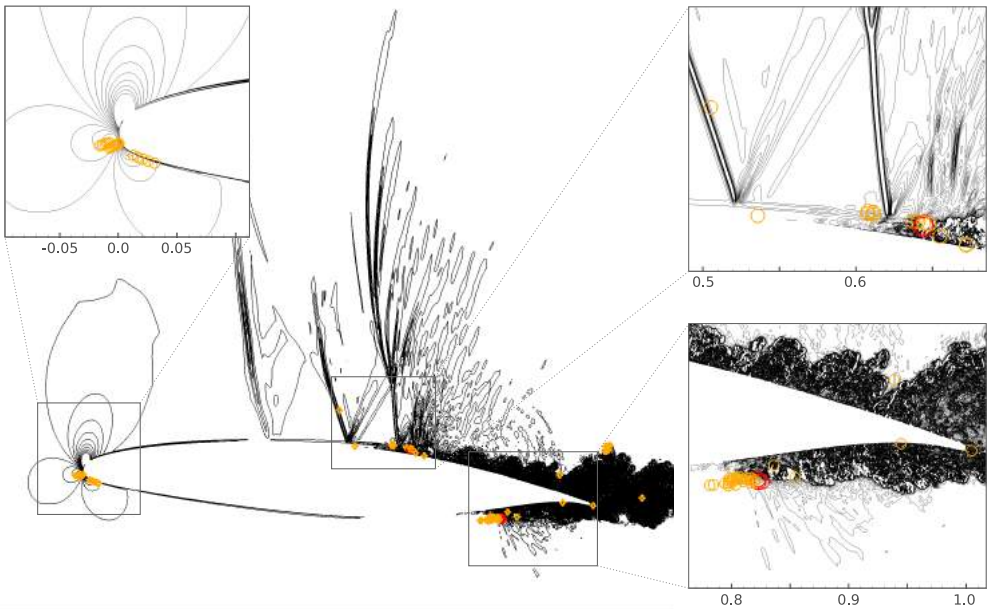

Fig. 12 Spectral error-indicators (orange and red for levels 2 and 3, respectively) for a snapshot of the reference simulation. The isocurves indicate axial pressure-gradient levels.

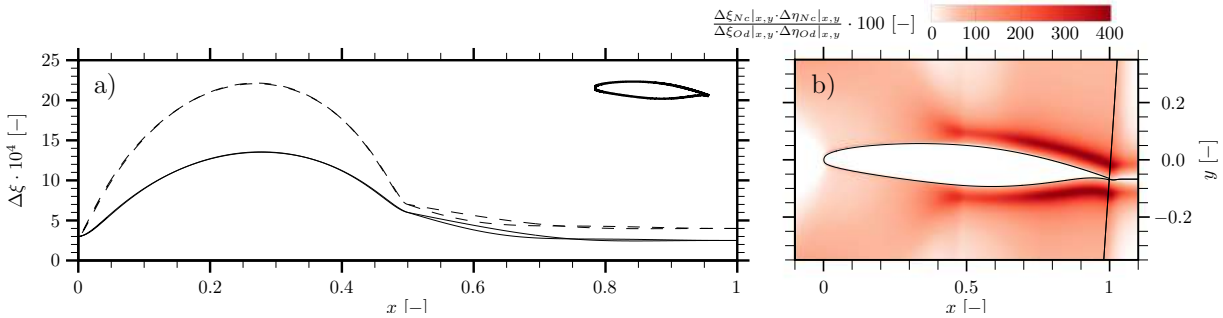

Fig. 13 (a) Grid spacing in the ξ-direction as a function of x. Dashed lines correspond to grid *Nc* and solid lines to the refined grid *Od*. (b) Contour plot of the ratio between local cell areas of grid *Nc* and *Od*.

with the reference solution. Due to an increased magnitude of the skin-friction coefficient in case $G2$ near $x \approx 0.5$ and a color map that is focused on flow separation ($C_f \approx 0$), the four local minima of the $St \approx 0.5$ cycle appear in the C_f-contours of figure 6(c) not as distinct as in figure 6(a) and (b). The top line plots of figure 6 show the total separation time t_{sep} for each case. The axial location of the statistical separation point and the fraction of flow separation in the aft section hardly change for the refined cases. In case $G2$, the flow is almost permanently separated close to half chord and both refined simulations show a slightly more distinct peak in flow separation over time at $x \approx 0.7$. The grid study suggests no significant qualitative changes compared to the reference simulations. Also the high-frequency Mach-wave pattern is observed in all cases. It should be noted that acoustic waves are not fully resolved in the potential flowfield (regions, where there are less than five grid points per wave length). Refinement of those regions is omitted, as it is not affecting the main objectives of our study. Nor is the wake fully resolved far downstream of the trailing edge. Table 2 summarizes averaged values of lift coefficient C_L and aerodynamic efficiency $\frac{\widetilde{C_L}}{\widetilde{C_D}}$, for all simulations. The time average as well as root-mean-square (RMS) of the fluctuations are calculated for the xy slice at $z = 0$ according to

$$q'_{RMS} = \sum_{t=T_1}^{T_2} \sqrt{\frac{\left(q_{(t)} - \overline{q}|_{T_1}^{T_2}\right)^2}{T_2 - T_1}}, \tag{6}$$

where T_1 and T_2 denote the beginning and end of the considered time interval. Additionally, the largest difference between peak and valley in the C_L signal is denoted by $(\Delta C_L)_{max}$. The simulations for the grid study were run over 8 time units, corresponding to one low-frequency cycle. The statistical convergence of the time- and span-averaged flowfield is evaluated in figure 11.The mean deviation of the statistical values for the reference case $C0$, considering three different time intervals, are given in the last line of table 2 and represent the statistical uncertainty due to the finite size of the sampling interval. The refined cases show only marginal deviations in the mean lift-coefficient, whereas the more sensitive RMS value for case $G2$ is about 10% higher. This is mainly due to the $(\Delta C_L)_{max}$, but still lower than the variation comparing different time intervals. The difference in the RMS values between cases $C0$ and $C1$ (wide domain) is higher, since the flowfield went through a transient, as the periodicity of the starting solution was breaking down. However, the deviation is still in the order of magnitude of the uncertainty due to the limited averaging interval and all the phenomena that were discussed in section IV are present.

Conclusions

DNS of the flow around Dassault Aviation's V2C airfoil at an angle of attack of 4° have been carried out at Re = 500,000 and $M = 0.7$, considering a spanwise domain width of $0.05c$. A wide range of flow phenomena are observed. In contrast to experiments of [18] at significantly higher Reynolds numbers, no permanent shock wave is detected. On the pressure side, upstream-travelling shock waves are generated with frequencies (Strouhal numbers)

Tag	*Grid size*	L_z	*Interval*	$\overline{C_L}$	$\overline{\frac{C_L}{C_D}}$	$C'_{L,RMS}$	$\left(\frac{C_L}{C_D}\right)'_{RMS}$	$(\Delta C_L)_{max}$	*Remarks*
$C0$	$1.07 \cdot 10^{-9}$	0.05	0 – 25	0.386	15.9	0.0260	1.386	0.1086	reference case (25 TU)
$C0$	$1.07 \cdot 10^{-9}$	0.05	13 – 21	0.393	15.8	0.0329	1.588	0.1086	reference case (8 TU)
$C1$	$5.35 \cdot 10^{-9}$	0.25	13 – 21	0.411	15.8	0.0233	1.300	0.0809	extended domain
$C0$	$1.07 \cdot 10^{-9}$	0.05	0.4 – 8.4	0.381	15.6	0.0186	1.042	0.0673	reference case (8 TU)
$G1$	$1.68 \cdot 10^{-9}$	0.05	0.4 – 8.4	0.385	16.1	0.0153	1.032	0.0573	refined xy-plane
$G2$	$1.78 \cdot 10^{-9}$	0.05	0.4 – 8.4	0.387	15.8	0.0206	1.023	0.0732	refined in z-direction
$\left(\left\|C0\|_{0.4}^{8.4} - C0\|_{13}^{21}\right\|\right) / \left(2 \cdot C0\|_0^{25}\right)$				0.016	0.006	0.275	0.197	0.190	reference deviation

Table 2 Statistical overview of the aerodynamic coefficients for an xy-plane at $z = 0$.

around $St \approx 0.5$. That frequency range is prominent in recirculation regions at the half chord position on the suction-side. Analysis of the surface-density (which corresponds to surface-pressure at the isothermal wall) over 25 time units suggests a separate low-frequency phenomenon at $St = 0.12$, corresponding to variations in the lift coefficient at the same Strouhal number. Oscillations at those frequencies are typical for transonic buffet phenomena that occur on modern wings at non-zero incidence, classified as type-II shock buffet[5]. Similar buffet-frequencies are reported for experimental investigations on the $V2C$ airfoil at higher Reynolds numbers. The laminar/turbulent transition mechanism on both sides is similar to the mechanism found by [15]. Large 2D roll-ups caused by Kelvin Helmholtz instabilities trigger secondary instabilities forming longitudinal vortices, called ribs [37]. Stretching of these rib vortices by co-rotating KH roll-ups promotes a rapid breakdown to turbulence. In the separated boundary layer, slowly upstream-moving structures can be observed on both sides, as well as high-frequency acoustic waves generating a Mach-wave pattern in the potential flow. An extensive grid dependency study confirmed the grid independence of all discussed flow phenomena, suggesting a sufficiently resolved flowfield for the reference case. This is supported by the partially converged grid study of [16], where the biggest grid has a comparable resolution to our reference grid. The simulation of a five times wider domain indicates also convective 2D KH roll-ups and low-frequency oscillations. Based on a study of linear instabilities in the flow around a high-pressure turbine vane cascade at similar flow conditions, [30] suggest that the growth rates of KH instabilities, similar to those discussed in the current work, do not show high sensitivity to spanwise wave numbers. Therefore, the reference simulation is expected to capture the essential flow features. Finally, the time- and span-averaged flowfield of the reference simulation is sufficiently converged, allowing future linear stability analysis of the mean flow.

Acknowledgement

We would like to acknowledge the UK National Supercomputing Service ARCHER (Leadership grant entitled "Transonic flow over an aerofoil"), EPSRC (grant EP/M022692/1 entitled "Unsteady aerodynamics of wings in extreme conditions"), UKTC (grant EP/L000261/1) and the Iridis cluster of the University of Southampton for the computational resources. MZ was supported by EPSRC (award reference 1665277). Pertinent data will be made available upon publication.

References

[1] Stack, J., and von Doenhoff, A. E., "Tests of 16 Related Airfoils at High Speeds," Tech. rep., 1934.

[2] Nieuwland, G. Y., and Spee, B. M., "Transonic Airfoils: Recent Developments in Theory, Experiment, and Design," *Annual Review of Fluid Mechanics*, Vol. 5, No. 1, 1973, pp. 119–150. doi:10.1146/annurev.fl.05.010173.001003, URL https://doi.org/10.1146/annurev.fl.05.010173.001003.

[3] Kehoe, M. W., "Overview Testing of Flight Flutter Testing," *NASA Technical Memorandum*, Vol. 4720, 1995.

[4] Lee, B., "Self-sustained shock oscillations on airfoils at transonic speeds," *Progress in Aerospace Sciences*, Vol. 37, No. 2, 2001, pp. 147–196. doi:10.1016/S0376-0421(01)00003-3, URL http://linkinghub.elsevier.com/retrieve/pii/S0376042101000033.

[5] Giannelis, N. F., Vio, G. A., and Levinski, O., "A review of recent developments in the understanding of transonic shock buffet," *Progress in Aerospace Sciences*, Vol. 92, No. May, 2017, pp. 39–84. doi:10.1016/j.paerosci.2017.05.004, URL http://dx.doi.org/10.1016/j.paerosci.2017.05.004http://linkinghub.elsevier.com/retrieve/pii/S0376042117300271.

[6] Pearcey, H. H., "A method for the prediction of the onset of buffeting and other separation effects from wind tunnel tests on rigid models," *AGARD Report*, Vol. 223, 1958.

[7] Bouhadji, A., and Braza, M., "Organised modes and shock–vortex interaction in unsteady viscous transonic flows around an aerofoil," *Computers & Fluids*, Vol. 32, No. 9, 2003, pp. 1233–1260. doi:10.1016/S0045-7930(02)00100-7, URL http://linkinghub.elsevier.com/retrieve/pii/S0045793002001007.

[8] Hoarau, Y., Braza, M., Ventikos, Y., Faghani, D., and Tzabiras, G., "Organized modes and the three-dimensional transition to turbulence in the incompressible flow around a NACA0012 wing," *Journal of Fluid Mechanics*, Vol. 496, No. 2003, 2003, pp. 63–72. doi:10.1017/S0022112003006530.

[9] Hoarau, Y., Faghani, D., Braza, M., and Perrin, R., "Direct Numerical Simulation of the Three-Dimensional Transition to Turbulence in the Incompressible Flow around a Wing," *Flow, Turbulence, and Combustion*, Vol. 71, 2003, pp. 119–132. doi:10.1023/B:APPL.0000014932.28421.9e.

[10] Vinuesa, R., Hosseini, S. M., Hanifi, A., Henningson, D. S., and Schlatter, P., "Direct numerical simulation of the flow around a wing section using high-order parallel spectral methods," *International Symposium on Turbulence and Shear Flow Phenomena*, Vol. 0, No. JANUARY, 2016, pp. 1–6. doi:10.1016/j.ijheatfluidflow.2016.02.001, URL http://dx.doi.org/10.1016/j.ijheatfluidflow.2016.02.001.

[11] Szubert, D., Asproulias, I., Grossi, F., Duvigneau, R., Hoarau, Y., and Braza, M., "Numerical study of the turbulent transonic interaction and transition location effect involving optimisation around a supercritical aerofoil," *European Journal of Mechanics - B/Fluids*, Vol. 55, 2016, pp. 380–393. doi:10.1016/j.euromechflu.2015.09.007, URL http://linkinghub.elsevier.com/retrieve/pii/S0997754615300285.

[12] Sznajder, J., and Kwiatkowski, T., "Analysis of effects of shape and location of micro-turbulators on unsteady shockwave-boundary layer interactions in transonic flow," *Journal of KONES Powertrain and Transport*, Vol. 23, No. 2, 2016, pp. 373–380. doi:10.5604/12314005.1213755, URL http://10048.indexcopernicus.com/abstracted.php?level=5{&}ICID=1213755http://linkinghub.elsevier.com/retrieve/pii/S0997754615300285.

[13] Bourdet, S., Bouhadji, A., Braza, M., and Thiele, F., "Direct Numerical Simulation of the Three-Dimensional Transition to Turbulence in the Transonic Flow around a Wing," *Flow, Turbulence and Combustion (formerly Applied Scientific Research)*, Vol. 71, No. 1-4, 2003, pp. 203–220. doi:10.1023/B:APPL.0000014932.28421.9e, URL http://link.springer.com/10.1023/B:APPL.0000014932.28421.9e.

[14] Shan, H., Jiang, L., and Liu, C., "Direct numerical simulation of flow separation around a NACA 0012 airfoil," *Computers & Fluids*, Vol. 34, No. 9, 2005, pp. 1096–1114. doi:10.1016/j.compfluid.2004.09.003.

[15] Jones, L., "Numerical studies of the flow around an airfoil at low Reynolds number," Ph.D. thesis, 2008.

[16] Gageik, M., Klioutchnikov, I., and Olivier, H., "Comprehensive mesh study for a Direct Numerical Simulation of the transonic flow at Rec = 500,000 around a NACA 0012 airfoil," *Computers and Fluids*, Vol. 122, 2015, pp. 153–164. doi:10.1016/j.compfluid.2015.08.030, URL http://dx.doi.org/10.1016/j.compfluid.2015.08.030.

[17] Balakumar, P., "Direct Numerical Simulation of Flows over an NACA-0012 Airfoil at Low and Moderate Reynolds Numbers," *47th AIAA Fluid Dynamics Conference*, , No. June, 2017, pp. 1–19. doi:10.2514/6.2017-3978, URL https://arc.aiaa.org/doi/10.2514/6.2017-3978.

[18] Placek, R., and Ruchała, P., "The flow separation development analysis in subsonic and transonic flow regime of the laminar airfoil," *Transportation Research Procedia*, Vol. 29, No. Figure 1, 2018, pp. 323–329. doi:10.1016/j.trpro.2018.02.029, URL http://linkinghub.elsevier.com/retrieve/pii/S2352146518300334.

[19] Davidson, T., "Effect of incoming boundary layer state on flow development downstream of normal shock wave - boundary layer interactions," Phd thesis, University of Cambridge, 2016.

[20] Crouch, J. D., Garbaruk, A., and Magidov, D., "Predicting the onset of flow unsteadiness based on global instability," *Journal of Computational Physics*, Vol. 224, No. 2, 2007, pp. 924–940. doi:10.1016/j.jcp.2006.10.035.

[21] Yao, Y., Shang, Z., Castagna, J., Johnstone, R., Jones, L., Redford, J., Sandberg, R., Sandham, N., Suponitsky, V., and De Tullio, N., "Re-Engineering a DNS Code for High-Performance Computation of Turbulent Flows," *47th AIAA Aerospace Sciences Meeting including The New Horizons Forum and Aerospace Exposition*, American Institute of Aeronautics and Astronautics, Reston, Virigina, 2009. doi:10.2514/6.2009-566, URL http://arc.aiaa.org/doi/10.2514/6.2009-566.

[22] Carpenter, M. H., Nordström, J., and Gottlieb, D., "A Stable and Conservative Interface Treatment of Arbitrary Spatial Accuracy," *Journal of Computational Physics*, Vol. 148, No. 2, 1999, pp. 341–365. doi:10.1006/jcph.1998.6114, URL http://linkinghub.elsevier.com/retrieve/pii/S0021999198961149.

[23] Sandhu, H., and Sandham, N., "Boundary conditions for spatially growing compressible shear layers," Tech. rep., Faculty of Engineering, Queen Mary and Westfield College, University of London, 1994.

[24] Sandberg, R. D., and Sandham, N. D., "Nonreflecting Zonal Characteristic Boundary Condition for Direct Numerical Simulation of Aerodynamic Sound," *AIAA Journal*, Vol. 44, No. 2, 2006, pp. 402–405. doi:10.2514/1.19169, URL http://arc.aiaa.org/doi/10.2514/1.19169.

[25] Jones, L. E., Sandberg, R. D., and Sandham, N. D., "Direct numerical simulation of an airfoil with unsteady wake," *European Conference on Computational Fluid Dynamics*, 2006, pp. 1–18.

[26] Zauner, M., and Sandham, N. D., "Multiblock structured grids for direct numerical simulations of transonic wing sections," *Proceedings of the Tenth International Conference on Computational Fluid Dynamics*, Barcelona, 2018.

[27] Jones, L., Sandberg, R., and Sandham, N., "Direct numerical simulations of forced and unforced separation bubbles on an airfoil at incidence," *Journal of Fluid Mechanics*, Vol. 602, 2008, pp. 175–207. doi:10.1017/S0022112008000864, URL http://eprints.soton.ac.uk/55698/.

[28] Zhang, W., and Samtaney, R., "Assessment of spanwise domain size effect on the transitional flow past an airfoil," *Computers and Fluids*, Vol. 124, 2016, pp. 39–53. doi:10.1016/j.compfluid.2015.10.008, URL http://dx.doi.org/10.1016/j.compfluid.2015.10.008.

[29] Wheeler, A. P. S., Sandberg, R. D., Sandham, N. D., Pichler, R., Michelassi, V., and Laskowski, G., "Direct Numerical Simulations of a High-Pressure Turbine Vane," *Journal of Turbomachinery*, Vol. 138, No. 7, 2016, p. 071003. doi:10.1115/1.4032435, URL http://turbomachinery.asmedigitalcollection.asme.org/article.aspx?doi=10.1115/1.4032435.

[30] Zauner, M., Sandham, N. D., Wheeler, A. P. S., and Sandberg, R. D., "Linear Stability Prediction of Vortex Structures on High Pressure Turbine Blades," *International Journal of Propulsion and Power*, Vol. 2, No. 8, 2017. doi:10.3390/ijtpp2020008.

[31] Leweke, T., Le Dizès, S., and Williamson, C. H., "Dynamics and Instabilities of Vortex Pairs," *Annual Review of Fluid Mechanics*, Vol. 48, No. 1, 2016, pp. 507–541. doi:10.1146/annurev-fluid-122414-034558, URL http://www.annualreviews.org/doi/10.1146/annurev-fluid-122414-034558.

[32] Mitchell, B., Lele, S., and Moin, P., "Direct computation of the sound from a compressible co-rotating vortex pair," *30th Aerospace Sciences Meeting and Exhibit*, Vol. 285, American Institute of Aeronautics and Astronautics, Reston, Virigina, 1992, pp. 181–202. doi:10.2514/6.1992-374, URL http://arc.aiaa.org/doi/10.2514/6.1992-374.

[33] Singer, B. A., Brentner, K. S., Lockard, D. P., and Lilley, G. M., "Simulation of acoustic scattering from a trailing edge," Vol. 230(3), 2000, pp. 541–560. doi:10.1006/jsvi.1999.2628.

[34] Tijdeman, H., "On the Motion of Shock Waves on an Airfoil with Oscillating Flap," *Symposium Transsonicum II. International Union of Theoretical and Applied Mechanics*, , No. September 1975, 1975. doi:https://doi.org/10.1007/978-3-642-81005-3_4.

[35] Anderson Jr, J., *Fundamentals of Aerodynamics*, Vol. Third Edit, 1985. doi:10.1036/0072373350, URL http://scholar.google.com/scholar?hl=en{&}btnG=Search{&}q=intitle:Fundamentals+of+Aerodynamics{#}0.

[36] Zauner, M., De Tullio, N., and Sandham, N., "Unsteady behaviour in direct numerical solutions of transonic flow around an airfoil." *2018 Fluid Dynamics Conference*, American Institute of Aeronautics and Astronautics, Reston, Virginia, 2018, pp. 1–14. doi:10.2514/6.2018-2911, URL https://arc.aiaa.org/doi/10.2514/6.2018-2911.

[37] Hussain, A. K. M. F., "Coherent structures and turbulence," *Journal of Fluid Mechanics*, Vol. 173, No. -1, 1986, p. 303. doi:10.1017/S0022112086001192, URL http://www.journals.cambridge.org/abstract{_}S0022112086001192.

[38] Rogers, M. M., and Moser, R. D., "The three-dimensional evolution of a plane mixing layer: The Kelvin-Helmholtz rollup," *Journal of Fluid Mechanics*, Vol. 243, 1992, pp. 183–226. doi:10.1017/S0022112092002696.

[39] Babucke, A., Kloker, M., and Rist, U., "DNS of a plane mixing layer for the investigation of sound generation mechanisms," *Computers and Fluids*, Vol. 37, No. 4, 2008, pp. 360–368. doi:10.1016/j.compfluid.2007.02.002.

[40] Bernal, L. P., and Roshko, A., "Streamwise vortex structure in plane mixing layers," *Journal of Fluid Mechanics*, Vol. 170, 1986, pp. 499–252. doi:10.1017/S002211208600099X, URL http://www.journals.cambridge.org/abstract{_}S002211208600099X.

[41] Placek, R., and Miller, M., "Wind Tunnel Tests of laminar-turbulent transition influence on basic aerodynamic characteristics of laminar airfoil in transonic flow regime," Tech. rep., Institute of Aviation in Warsaw, 2016.

[42] Jacobs, C. T., Zauner, M., De Tullio, N., Jammy, S. P., Lusher, D. J., and Sandham, N. D., "An error indicator for finite difference methods using spectral techniques with application to aerofoil simulation," *Computers & Fluids*, Vol. 168, 2018, pp. 67–72. doi:10.1016/j.compfluid.2018.03.065, URL http://linkinghub.elsevier.com/retrieve/pii/S0045793018301695.

[43] Barber, C. B., Dobkin, D. P., and Huhdanpaa, H., "The quickhull algorithm for convex hulls," *ACM Transactions on Mathematical Software*, Vol. 22, No. 4, 1996, pp. 469–483. doi:10.1145/235815.235821, URL http://portal.acm.org/citation.cfm?doid=235815.235821.